Magnetization steps in $Zn_{1-x}Mn_xO$: Four largest exchange constants and single-ion anisotropy

X. Gratens, V. Bindilatti,* and N. F. Oliveira, Jr.
Instituto de Física, Universidade de São Paulo, Caixa Postal 66.318, 05315-970 São Paulo, São Paulo, Brazil

Y. Shapira†
Department of Physics and Astronomy, Tufts University, Medford, Massachusetts 02155, USA

S. Foner
Francis Bitter Magnet Laboratory, Massachusetts Institute of Technology, Cambridge, Massachusetts 02139, USA

Z. Golacki
Institute of Physics, Polish Academy of Sciences, Al. Lotnikow 32/46, 02-668, Warsaw, Poland

T. E. Haas
Department of Chemistry, Tufts University, Medford, Massachusetts 02155, USA
(Received 8 October 2003; published 17 March 2004)

Magnetization steps from Mn^{2+} pairs in several single crystals of $Zn_{1-x}Mn_xO$ ($0.0056 \leqslant x \leqslant 0.030$), and in one powder ($x=0.029$), were observed. They were used to determine the four largest exchange constants (largest J's), and the single-ion axial anisotropy parameter D. The largest two exchange constants, $J_1/k_B = -18.2 \pm 0.5$ K and $J_1'/k_B = -24.3 \pm 0.5$ K, were obtained from large peaks in the differential susceptibility, dM/dH, measured in pulsed magnetic fields H up to 500 kOe. These two largest J's are associated with the two inequivalent classes of nearest neighbors (NN's) in the wurtzite structure. The 29% difference between J_1 and J_1' is substantially larger than 13% in $Cd_{1-x}Mn_xS$ and 15% in $Cd_{1-x}Mn_xSe$. The pulsed-field data also indicate that, despite the direct contact between the samples and a superfluid-helium bath, substantial departures from thermal equilibrium occurred during the 7.4-ms pulse. The third- and fourth-largest J's were determined from the magnetization M at 20 mK, measured in dc magnetic fields H up to 90 kOe. Both field orientations $\mathbf{H} \| \mathbf{c}$ and $\mathbf{H} \| [10\bar{1}0]$ were studied. (The $[10\bar{1}0]$ direction is perpendicular to the c axis, $[0001]$.) By definition, neighbors which are not NN's are distant neighbors (DN's). The largest DN exchange constant (third-largest overall) has the value $J/k_B = -0.543 \pm 0.005$ K, and is associated with the DN at $\mathbf{r}=\mathbf{c}$. Because this is not the closest DN, this result implies that the J's do not decrease monotonically with the distance r. The second-largest DN exchange constant (fourth-largest overall) has the value $J/k_B \approx -0.080$ K. It is associated with one of the two classes of neighbors that have a coordination number $z_n=12$, but the evidence is insufficient for a definite unique choice. The dependence of M on the direction of $\mathbf{H}$ gives $D/k_B = -0.039 \pm 0.008$ K, in fair agreement with -0.031 K from earlier electron paramagnetic resonance work.

DOI: 10.1103/PhysRevB.69.125209 PACS number(s): 71.70.Gm, 75.50.Ee, 75.10.Jm, 75.60.Ej

I. INTRODUCTION

The most extensively studied diluted magnetic semiconductors (DMS's) are II-VI materials ($A^{II}B^{VI}$, where $A=$Zn, Cd, $B=$S,Se,Te) in which some of the cations have been replaced by manganese.[1] The magnetization-step (MST) method is one of the most effective techniques of measuring antiferromagnetic (AF) exchange constants in DMS's.[2,3] This technique has been used to determine nearest-neighbor (NN) and distant-neighbor (DN) exchange constants in several II-VI DMS's with the zinc-blende[4–6] and wurtzite[7–9] structures. Relevant theoretical treatments of these exchange constants include those in Refs. 10–12. In addition to exchange constants, the MST method gives information about magnetic anisotropies, and about the distribution of the magnetic ions in the crystal, on a length scale of several atomic dimensions.

The MST method probes the energy-level diagrams of small clusters of magnetic ions in DMS's with low concentration of magnetic ions. Inelastic scattering of neutrons from such small clusters (mainly pairs) is another powerful method of determining the *d-d* exchange constants in DMS's.[13–15] These two methods of accurately measuring exchange constants are complementary; each has its own advantages.

A new class of II-VI DMS's based on ZnO, especially $Zn_{1-x}Mn_xO$, has attracted attention recently because theoretical calculations suggested the possibility of ferromagnetism above 300 K in *p*-type samples.[16] Experimental works on epitaxial thin films of $Zn_{1-x}Mn_xO$ gave different results: ferromagnetism was reported in Ref. 17, but according to Ref. 18 the largest exchange constant is antiferromagnetic, $J/k_B \approx -15$ K. In the present work, MST's from several $Zn_{1-x}Mn_xO$ single crystals, and from one powder sample, were used to determine the largest four exchange constants. The single-ion axial anisotropy parameter D was also determined.

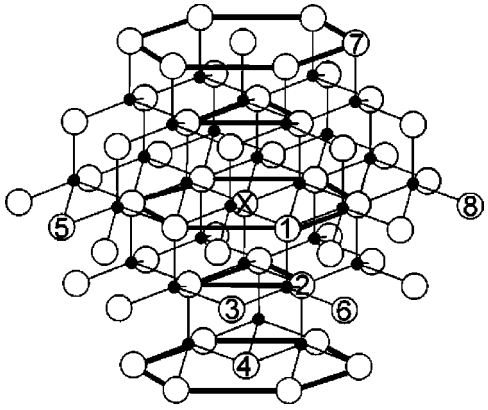

FIG. 1. The wurtzite crystal structure. The large white spheres are the cations, the small black spheres are the anions. The ''central cation'' is labeled as X. One example of each of the neighbor classes in Table I is indicated by the number n specifying that class.

TABLE I. Classification of neighbors in the vicinity of a ''central cation'' in the hcp cation structure. The neighbor class is specified by n. The distance of such a neighbor from the central cation, in the ideal hcp structure, is r_n. The coordination number z_n is the number of neighbors of class n which surround the central cation. The fourth row gives alternative designations for the exchange constants $J(n)$, e.g., the exchange constant $J(4)$ for a neighbor of the class $n=4$ is designated as J_3'. The superscripts ''in'' and ''out'' distinguish between equidistant but inequivalent neighbors: those in the same c plane and those in different c planes. The dipole-dipole interaction constant $(g\mu_B)^2/r_n^3$, expressed in kelvin, is for the lattice parameter a of ZnO, but using the ideal ratio $c/a=\sqrt{8/3}$.

n	1	2	3	4	5	6	7	8
r_n/a	1		$\sqrt{2}$	$\sqrt{8/3}$	$\sqrt{3}$		$\sqrt{11/3}$	2
z_n	6	6	6	2	6	12	12	6
$J(n)$	J_1^{in}	J_1^{out}	J_2	J_3'	J_3^{in}	J_3^{out}	J_4'	J_4
$\frac{(g\mu_B)^2}{r_n^3}$	0.073		0.026	0.017	0.014		0.010	0.009

II. CRYSTAL STRUCTURE AND CLASSIFICATION OF NEIGHBORS

A. Classification of neighbors by classes

The hexagonal wurtzite structure of ZnO (space group $P6_3mc$) is shown in Fig. 1. The cations (open circles) form a hexagonal close-packed (hcp) structure. The cation marked by X is chosen as the ''central cation.'' The other cations are often classified by their distances from the central cation, i.e., NN's, second neighbors, etc.[10] A major shortcoming of the classification by distance is that in the (ideal) hcp structure some equidistant cations are not equivalent from symmetry point of view. Equidistant but symmetry-inequivalent cations have different isotropic exchange constants.

The classification of neighbors by symmetry, instead of distance, is discussed in Refs. 2 and 3. In this classification, neighbors are divided into ''classes.'' Neighbors of the same class have the following property: When cation sites are occupied by magnetic ions, neighbors of the same class have the same isotropic (Heisenberg) exchange interaction with the magnetic ion at the central site. The exchange constant J is therefore the same for all neighbors of the same class. The underlying reason is that all pairs of cation sites consisting of the central site and a neighbor of a given class are related to each other by operations of the space group of the cation structure. Interactions other than isotropic exchange sometimes require distinctions between neighbors of the same class.[19]

Properties of several classes of neighbors are given in Table I. The number n, which is the same as in Ref. 3, specifies the neighbor class. Note that $n=1$ and $n=2$ are two inequivalent classes of NN's. As can be seen in Fig. 1, $n=1$ corresponds to ''in plane'' NN's (i.e., NN's which are in the same c plane), whereas $n=2$ corresponds to ''out of plane'' NN's. The distances in Table I are for the ideal hcp structure, with $c/a=\sqrt{8/3}$, where a is the NN distance. A neighbor of the symmetry class $n=3$ corresponds to a second neighbor in the classification by distance. Neighbors of class $n=4$ are reached from the central cation by moving a distance c along the c axis. They are the closest neighbors along the hexagonal direction. Neighbors of classes $n=5$ and $n=6$ are equidistant but are inequivalent by symmetry. The remaining neighbor classes in Table I, $n=7$ and $n=8$, are included in Fig. 1. The parameter z_n in Table I is the ''coordination number,'' i.e., the number of neighbors of class n surrounding the central cation.

The notation for the exchange constants J's associated with different neighbors has been evolving, to accommodate newer classifications of these J's. In early works, when neighbors were classified by their distance r, the notation for the J's also was based on distance: J_1 for NN's, J_2 for next-nearest (second) neighbors, J_3 for third neighbors, etc. For II-VI DMS's with the zinc-blende structure (fcc cation lattice) this notation is still quite useful because each of the eight shortest distances r is associated with a unique neighbor class n (see footnote 115 in Ref. 2). However, the distance-based notation is totally inadequate for DMS's with the wurtzite structure (hcp cation structure). In the ideal hcp structure, the shortest distance r already corresponds to two classes of NN's, with different J's.

An early apparent advantage of the distance-based notation followed from the prediction[10] that the magnitudes (sizes) of the J's decrease monotonically with increasing r. If true, this prediction would have made the classification by distance equivalent to a classification by size. However, later theories,[11,12] and recent experiments,[5,20] indicate that there is no simple correspondence between size and distance.

The different notations for the J's that are used in the present work serve different needs. The simplest notation $J(n)$ associates the J's with the neighbor classes n listed in Table I. For example, $J(4)$ is the exchange constant with a neighbor of the class $n=4$. The disadvantage of this notation is that neither the relevant distance r nor the ranking by size are immediately obvious.

An alternative notation, similar to that in Ref. 21, is given in the fourth row of Table I. This notation too is based on division of neighbors into symmetry classes, but it also gives

some information about the distance r. Instead of the number n, the neighbor class is specified by a combination of subscripts and superscripts. The information about distance is given by the numerical value of the subscript, which increases with increasing r. For the same subscript, the superscripts ''in'' and ''out'' are used to distinguish between equidistant but inequivalent neighbor classes. Thus, $J_1^{\rm in}$ and $J_1^{\rm out}$ are the J's for the two classes of NN's. A prime is added as a superscript to indicate that the distance r is approximately, but not exactly, the same as for an unprimed exchange constant with the same subscript. For example, the exchange constants for the neighbor classes $n=7$ and $n=8$, whose distances differ by only 4%, are designated as J_4' and J_4, respectively.

B. Classification of exchange constants by size

The preceding two notations for the J's were both based on the division of neighbors into symmetry *classes*. This classification, however, has a serious practical drawback. Quite often the magnitude (size) of an exchange constant is measured *before* the neighbor class with which it is associated is determined. Prior to such a determination, any notation based on the neighbor class is not useful. It is then more practical to adopt a notation that is based primarily on the ranking of the J's by size. In the present work, only the four largest J's were measured. The chosen designations of these J's in terms of their sizes are as follows.

(1) The largest two exchange constants are labeled J_1 and J_1', with J_1 chosen (arbitrarily) to be the smaller of the two. These two exchange constants are associated with the two inequivalent classes of NN's. In the present work it has not been determined which of the two corresponds to $J_1^{\rm in}$ and which to $J_1^{\rm out}$.

(2) By definition, any exchange constant J which is not associated with either of the two classes of NN's is a DN exchange constant. The largest DN exchange constant (third-largest overall) is called $J^{(2)}$, the second-largest DN exchange constant (fourth-largest overall) is called $J^{(3)}$.

The assignment of $J^{(2)}$ and $J^{(3)}$ to specific neighbor classes is a major task that will be discussed in detail.

III. EXPERIMENT

A. Samples

Single crystals of $Zn_{1-x}Mn_xO$ ($0.0056 \leqslant x \leqslant 0.030$) were grown by chemical vapor transport using chlorine as the transporting agent. The growth temperature was 900 °C. The Mn concentration x was obtained using three methods.

(1) From the Curie constant, obtained from a fit of the susceptibility between 200 and 300 K to a sum of a Curie-Weiss susceptibility and a constant χ_d representing the lattice diamagnetism. The values $S=5/2$ and $g=2.0016$ (Ref. 22) for the Mn^{2+} ion were used.

(2) From the apparent saturation value M_s of the magnetization. The determination of M_s (also known as the ''technical saturation value'') is discussed in Sec. V. The relation between x and M_s was discussed in Refs. 2 and 23, among others. This relation is based on the assumption of a random distribution of the Mn ions over the cation sites.

(3) From atomic emission spectroscopy with inductively coupled plasma.

TABLE II. Mn concentration, x, as obtained from (1) the apparent saturation value M_s, (2) the susceptibility between 200 and 300 K, and (3) atomic emission spectroscopy with inductively coupled plasma (ICP-AES). The ''best value'' (B.V.) is the value adopted in the text.

Sample	$x(M_s)$	x(Suscept.)	x(ICP-AES)	x(B.V.)
A	0.0056	0.0057	0.005	0.0056
B	0.0210	0.0208	0.021	0.021
C	0.0291	0.0286		0.029
D	0.0305	0.0283	0.030	0.030

Table II compares the results of the three methods. The good agreement indicates that the apparent saturation value M_s is consistent with a random distribution of the Mn ions. The last column in Table II gives the chosen values of x that will be used to label the various samples, namely, $x=0.0056$, 0.021, 0.029, and 0.030. These values will also be used in the data analysis.

X-ray powder diffraction data were obtained on small portions of the samples with $x=0.0056$, 0.021, and 0.030. These data were taken with a Bruker model ''D8 Discover with GADDS'' spectrometer, using Cu K_α radiation. All the powder diffraction patterns were in good agreement with the wurtzite structure (space group $P6_3mc$). No other crystallographic phase was detected.

The samples used in measurements of the magnetization M, and of the differential susceptibility dM/dH, had linear dimensions of 2 to 4 mm. The only exception was one set of pulsed-field data on a powder obtained by crushing the single crystal with $x=0.029$. Pulsed-field data on that single crystal were obtained before it was crushed.

B. Magnetization measurements

Three types of magnetization measurements were performed.

(1) The magnetization M at $T=20$ mK was measured in dc magnetic fields up to 90 kOe. These data were taken with a force magnetometer operating in a plastic dilution refrigerator. The experimental techniques were described earlier.[24] The magnetic field H was either parallel to the c axis, or parallel to the $[10\bar{1}0]$ direction (one of the directions perpendicular to the c axis.) The dc magnetic field was produced by a NbTi superconducting magnet. Several traces of M versus H, in both increasing and decreasing H, were taken for each experimental configuration. All such traces were similar, and showed no hysteresis. They were averaged in order to improve the signal to noise ratio in the final result.

(2) The magnetization M was measured at 0.65 K in dc fields up to 170 kOe. The samples were immersed in a liquid ^{3}He bath. A vibrating sample magnetometer operating in an 18-T superconducting magnet (Nb_3Sn wire) was used.[25]

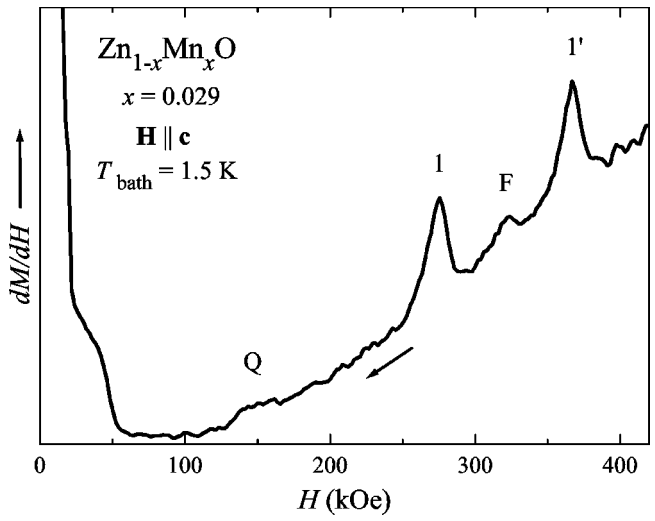

FIG. 2. Differential susceptibility dM/dH for a single crystal with $x=0.029$, measured in pulsed fields. These results are for the "down" portion of the pulse (decreasing H), with the magnetic field parallel to the c axis. The two large peaks, 1 and $1'$, are attributed to the two inequivalent NN pairs. The small peaks Q and F are discussed in the text.

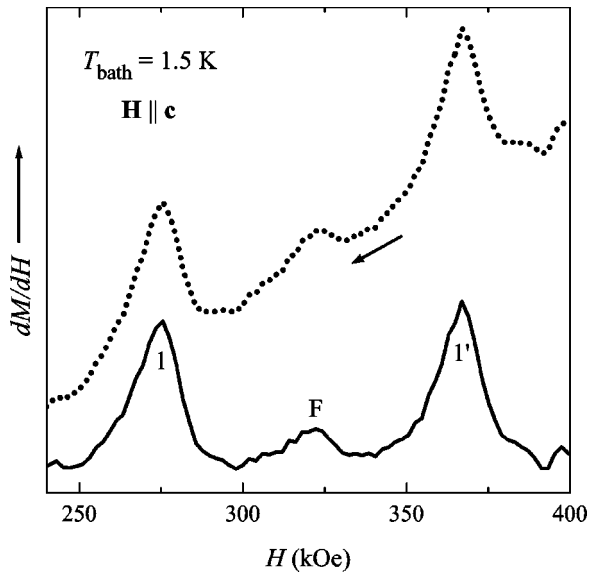

FIG. 3. The high-field portion of the results in Fig. 2. The raw experimental data, from Fig. 2, are represented by the dotted curve. The solid curve was obtained by subtracting a linear baseline. The two dominant peaks 1 and $1'$ are attributed to the two inequivalent NN pairs in the wurtzite structure.

Again, no hysteresis was observed, and traces were averaged to improve the signal to noise ratio.

(3) The differential susceptibility dM/dH was measured in pulsed magnetic fields up to 500 kOe. The experimental techniques were described earlier.[4] The pulse duration was 7.4 ms. The sample was in direct contact with a liquid ^{4}He bath maintained at a temperature $T_{bath}=1.5$ K. However, the data showed that despite the direct contact, the sample was not in thermal equilibrium with the liquid-helium bath during the pulse. Such nonequilibrium effects were found in earlier pulsed-field experiments.[26–29]

IV. NN EXCHANGE CONSTANTS FROM PULSED-FIELD DATA

A. NN exchange constants

Figure 2 shows dM/dH versus H for the single crystal with $x=0.029$. This trace is from the field-down portion of a pulse with a maximum field of 500 kOe. The two prominent peaks at high fields, labeled as 1 and $1'$, correspond to two MST's. The expanded view of these two peaks, shown in Fig. 3, indicates that both peaks have similar heights and widths. The maxima are at $H_1=275$ kOe and $H_1'=367$ kOe. These two peaks were not resolved in the up portion of this field pulse.

Pulsed-field measurements were also performed on single crystals with $x=0.021$ and 0.030, and on a powder obtained by crushing the single crystal with $x=0.029$ (after the data in Figs. 2 and 3 were obtained). In all cases the large peaks, 1 and $1'$, were resolved in the down portion of the pulse. However, in the up portion of the pulse these peaks were well resolved only in the following situations: (a) for the powder sample, in all field pulses, and (b) for the single crystal with $x=0.029$ when the maximum field was 420 kOe, as compared to 500 kOe for the pulse in Fig. 2. These results are explained later.

Based on the data in all samples, the two large MST's observed in pulsed fields are at $H_1=270\pm8$ kOe and $H_1'=362\pm8$ kOe. Because the uncertainties in these two values are correlated, the uncertainty in the difference is much smaller, i.e., $(H_1'-H_1)=92\pm2$ kOe. The average is $\overline{H_1}=(H_1'+H_1)/2=316\pm8$ kOe.

Earlier data for other DMS's with the wurtzite structure[7,8] showed that (a) each MST from NN pairs splits into a doublet, corresponding to the two inequivalent classes of NN's, and (b) the two corresponding exchange constants, J_1' and J_1, are the largest. The two large MST's at H_1' and H_1 are therefore attributed to the two inequivalent NN pairs.[30]

For Mn^{2+} pairs with intrapair exchange constant J, the magnetic fields H_n at the MST's are given by[2]

$$g\mu_B H_n = 2n|J|, \tag{1}$$

where $n=1,2,\ldots,5$. In the present case the calculated deviations from Eq. (1), caused by anisotropies and DN interactions, turn out to be smaller than the experimental uncertainties in H_1 and H_1'. Using $n=1$ and $g=2.0016$, we obtained $J_1/k_B=-18.2\pm0.5$ K and $J_1'/k_B=-24.3\pm0.5$ K. Unfortunately, it was not possible to conclude which of the two exchange constants is J_1^{in} and which is J_1^{out}. In the case of $Cd_{1-x}Mn_xSe$,[8] the smaller of the two NN exchange constants, defined here as J_1, was identified as J_1^{out}, and the larger as J_1^{in}. This identification was based on the effect of the Dzyaloshinkii-Moriya (DM) interaction on the widths of the MST's, and it also agreed with Larson's prediction.[31] In the present work the effect of the DM interaction was not apparent in the data, presumably because this interaction de-

creases rapidly as the atomic number of the *anion* decreases, i.e., much smaller for oxygen than for selenium.[32] Although direct evidence is lacking, based on the experimental result for $Cd_{1-x}Mn_xSe$ and on the theory, we speculate that in the present material too, $J_1 = J_1^{out}$ and $J_1' = J_1^{in}$.

As discussed earlier,[8] the dominant superexchange path for both classes of NN's, which is through the intervening anion, is the same. The difference between J_1^{in} and J_1^{out} is attributed to differences in the other exchange paths whose contribution is smaller. In the present material $\Delta\overline{J_1} = |J_1^{in} - J_1^{out}|$ is 29% of the average $\overline{J_1}/k_B = -21.2 \pm 0.5$ K. This percentage difference should be compared to 13% in $Cd_{1-x}Mn_xS$, and 15% in $Cd_{1-x}Mn_xSe$.[7,8]

B. Other features of the pulsed-field data

Figure 2 also shows two small peaks, labeled as *Q* and *F*. Computer simulations indicate that these peaks are due in part to MST's from quartets (tetramers). Each of these quartets consists of four spins that are coupled by some combination of J_1 and/or J_1' exchange bonds. Other possible contributions to these small peaks may be due to cross-relaxation processes that can occur in the absence of equilibrium.[29,33,34] The nonequilibrium behavior in pulsed fields, including cross relaxation, will be discussed in a later publication. Very briefly, the cross-relaxation processes that may contribute to *Q* are similar to those discussed in Ref. 34 in connection with the second-harmonic peak $P_{1/2}$. The cross-relaxation process that may contribute to *F* involves two NN pairs of different classes. The latter process is most rapid at $\overline{H_1} = (H_1' + H_1)/2$, where the energy separation between the two lowest levels for one class of NN pair matches that for the other class of NN pair.

The widths of peaks 1 and 1′ provide convincing evidence for other types of nonequilibrium processes, associated with a phonon bottleneck, which restricts the sample-to-bath heat flow.[27,28,35–38] From Fig. 3, the full width at half height of either of these two peaks is 14 kOe. This value should be compared with a minimum equilibrium width of 39 kOe at $T_{bath} = 1.5$ K. In addition to narrow widths, peaks 1 and 1′ also show a pronounced asymmetry which is characteristic of nonequilibrium behavior resulting from a phonon bottleneck. The 14-kOe width at half height is the sum of 5.5 kOe from the rise and 8.5 kOe from the fall. (The data in Fig. 3 are for decreasing *H*, so that the rise corresponds to fields above the maximum of dM/dH, and the fall corresponds to fields below the maximum.) Both the narrowing and the asymmetry are predicted from models for the phonon bottleneck.

The phonon bottleneck also accounts for the difficulty of resolving the peaks 1 and 1′ during the up portion of the field pulse. At the beginning of the pulse the magnetocaloric effect associated with the alignment of the singles causes the sample to warm. This heating is basically the inverse of cooling by adiabatic demagnetization, except that it is not fully adiabatic. To observe the peaks 1 and 1′, much of this heat must be transferred to the bath before these peaks are reached. In the up portion of the pulse the peaks are reached earlier than in the down portion. Apparently, in the case of the single crystals an insufficient amount of heat was transferred before reaching these peaks on the way up. The peaks were therefore not resolved in the up portion of the pulse. Lowering the maximum field of the pulse leads to a slight delay of the time when the peaks are reached on the way up, which improves the chance of resolving these peaks. A more drastic change occurs when a single crystal is crushed into powder. The resulting much larger surface to volume ratio improves the sample-to-bath heat flow substantially, and the peaks are also resolved in the up portion of the pulse.

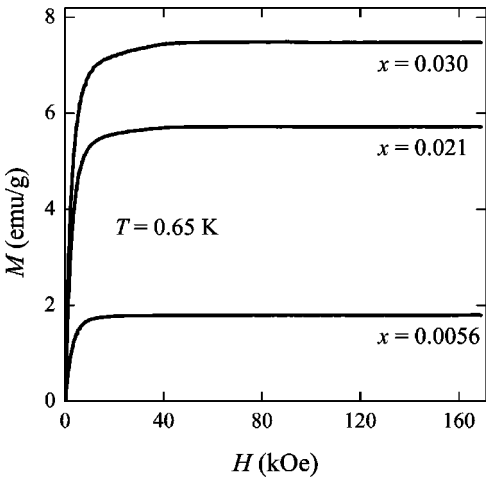

FIG. 4. Magnetization traces for $Zn_{1-x}Mn_xO$ crystals with $x = 0.0056$, 0.021, and 0.030 at $T = 0.65$ K. These data were taken in dc magnetic fields. A (minor) correction for the lattice diamagnetism is included.

Another phenomenon seen in Fig. 2 is that (for decreasing *H*) a rapid rise of dM/dH occurs below about 50 kOe. This rise is due to MST's from clusters in which the spins are coupled by DN exchange constants. The determination of these DN exchange constants is the main topic in the remainder of the paper.

V. DC MAGNETIZATION AT 0.65 K

Figure 4 shows magnetization curves at 0.65 K, measured in dc magnetic fields up to 170 kOe. As already noted, there was no hysteresis in any of the data taken in dc fields. The curves in Fig. 4 exhibit the expected behavior.[2] Above 50 kOe the magnetization *M* shows an apparent saturation (''technical saturation''). The apparent saturation value M_s is lower than the true saturation value M_0. The latter is expected to be reached in fields substantially above 170 kOe. The relation between M_s and *x* was used in Sec. III as one of the three methods of determining *x*. An expanded view of the upper portion of each of the curves in Fig. 4 does not show any MST between 50 and 170 kOe. (The magnetization change associated with the small peak *Q* in Fig. 2 is estimated to be about 0.2%. This small change was not resolved in any of the dc data for $x \leqslant 0.03$). The absence of detectable MST's in the dc data between 50 and 170 kOe indicates that all MST's from DN pairs occur below 50 kOe.

A feature of Fig. 4 which is most obvious for $x = 0.030$ is

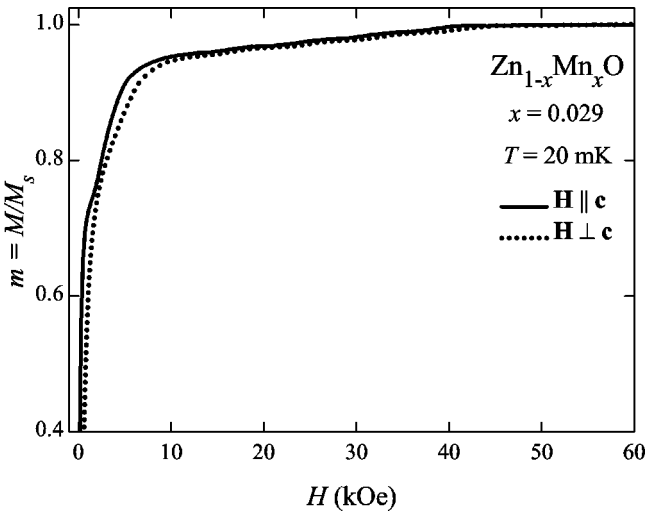

FIG. 5. Magnetization traces for $x=0.029$ measured at $T=20$ mK with $\mathbf{H}\perp\mathbf{c}$ (along the $[10\bar{1}0]$ direction) and $\mathbf{H}\|\mathbf{c}$. The magnetization was corrected for the lattice diamagnetism and normalized to its technical saturation value M_s.

a magnetization ''ramp'' ending slightly above 40 kOe. Magnetization ramps are produced by the coalescence of broadened MST's.[2] The ramp ending just above 40 kOe is due to the coalescence of MST's from clusters involving the largest DN exchange constant, defined earlier as $J^{(2)}$. These MST's were not resolved at 0.65 K, but were resolved at 20 mK.

VI. DN EXCHANGE CONSTANTS AND SINGLE-ION ANISOTROPY FROM 0.02-K DATA

A. Overall view of the dc magnetization at 20 mK

Figure 5 shows 20-mK data for $x=0.029$, taken both with $\mathbf{H}\|\mathbf{c}$ and $\mathbf{H}\perp\mathbf{c}$. These data are normalized to the technical saturation value M_s, and are corrected for the lattice diamagnetism. Expanded views of portions of these data are shown in Fig. 6. The main features are the following

(1) M rises quickly at low fields. This initial fast rise is typical. It is mainly due to the alignment of singles (Mn^{2+} ions with no significant exchange coupling to other Mn^{2+} ions).[2]

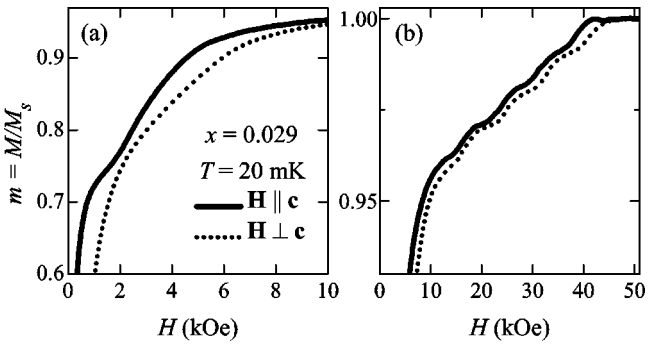

FIG. 6. Expanded views of (a) the low-field portion, and (b) the high-field portion of the magnetization traces in Fig. 5.

(2) The initial fast rise of M is followed by a ramp which ends near 5 or 6 kOe, depending on field direction. This ramp is shown more clearly in the expanded view of Fig. 6(a).

(3) A second ramp, smaller in height but spread over a larger field interval, follows the first ramp. The second ramp ends near 40 kOe. Just above this field, M reaches technical saturation.

(4) The magnetization depends on field direction. This anisotropic behavior is more obvious at low H.

Each of the two ramps is due to the coalescence of broadened MST's.[2] A well-defined ramp usually corresponds to one series of MST's. The high-field end of such a ramp is near the last MST from this series, and it can be used to estimate the relevant exchange constant J. A more accurate value for J can be obtained if the MST's on the ramp are well resolved.

The end of the second ramp, near 40 kOe, leads to the estimate $J^{(2)}/k_B \approx -0.5$ K for the largest DN exchange constant. The end of the first ramp, near 6 kOe, gives $J^{(3)}/k_B \approx -0.08$ K. To improve on these rough estimates it is necessary to examine the MST's which give rise to each ramp, taking into account the relevant weak anisotropic interactions.

B. Cluster models and anisotropies

Cluster models play a key role in analysis of MST's involving DN exchange interactions.[2] Detailed information about cluster models and their statistical properties is given in Ref. 3. In the present work, only the largest two DN exchange constants, $J^{(2)}$ and $J^{(3)}$, were determined. The cluster models that were used in the data analysis depended on the field range of the data.

(1) For fields below 8 kOe, both $J^{(2)}$ and $J^{(3)}$ are important. These exchange constants correspond to two classes of DN's, but the identity of neither of these two classes was known at the beginning of the analysis. Therefore, the cluster models used for this field range included (a) the two classes of NN's and (b) any possible two classes of DN's selected from the six classes listed in Table I.

(2) Because the magnetization above 10 kOe is hardly affected by $J^{(3)}$, the cluster models for the field range from 10 to 50 kOe involved only one class of a DN associated with $J^{(2)}$, and the two NN classes associated with J_1 and J_1'. All six possible choices for the class for the DN were tried.

(3) Analysis of the data between 50 kOe and 90 kOe was based primarily on a model which included only the two NN exchange constants. Simulations of the magnetization curves showed that in this field range the effects of the DN exchange constants $J^{(2)}$ and $J^{(3)}$ were very small.

In addition to the exchange interactions two anisotropies were also included in the analysis: single-ion anisotropy and dipole-dipole (dd) anisotropy. The effects of these anisotropies on the MST's (or ramp) from pairs become more pronounced as the magnitude $|J|$ of the relevant intrapair exchange constant decreases. That is, the effects caused by the anisotropies are very small for the MST's originating from NN pairs of either class; small but easily detected for the

MST's (ramp) from pairs involving $J^{(2)}$; and very pronounced for the MST's (ramp) from pairs involving $J^{(3)}$.

The single-ion anisotropy can be described by the Hamiltonian

$$DS_z^2+\frac{a}{6}(S_x^4+S_y^4+S_z^4),$$

where the z direction is along the c axis. From electronic paramagnetic resonance (EPR) at 77 K, $D/k_B=-31$ mK and $a/k_B=0.3$ mK.[22] Because the term involving a is relatively small, it was neglected in the present work. Values of the dd anisotropy constant for different classes of pairs are given in Table I. They are based on a simple model in which the two spins in a pair are represented by two points separated by r_n.

C. Results at 20 mK and their analysis

1. Objectives

The two objectives of the experiments at 20 mK were (1) to determine the values of $J^{(2)}$, $J^{(3)}$, and D, and (2) to identify the DN classes associated with $J^{(2)}$ and $J^{(3)}$. The analysis consisted of a number of steps taken in sequence. In what follows, each step in this sequence is outlined, and the results are summarized. The main assumption in the analysis is that the Mn ions are randomly distributed over the cation sites.

2. Procedures for identifying DN classes

The general procedure of associating DN constants of known magnitudes with different possible classes of DN's involves comparisons between experimental magnetization curves and computer simulations.[2,5] Separate simulations are carried out for all competing possibilities for the DN classes. The six DN classes listed in Table I lead to $6\times5=30$ possibilities for the two DN classes associated with $J^{(2)}$ and $J^{(3)}$. (Interchanging the order of the two classes of DN's leads to a new possibility.)

In the present work these laborious simulations were postponed, because a preliminary identification of the DN classes was possible based on a simpler, and more physical, procedure. Two favorable circumstances permitted the simpler procedure: a large difference in the magnitudes of $J^{(2)}$ and $J^{(3)}$, and the availability of data for a sample with a very small x.

For the lowest Mn concentration, $x=0.0056$, the ramp which ends near 40 kOe is due primarily to $J^{(2)}$ pairs. To a good approximation, the total magnetization rise $\Delta M^{(2)}$ associated with this ramp is therefore related to the fraction of Mn ions which are in such pairs. This fraction can be calculated for any possible choice of the DN class associated with $J^{(2)}$, so that $\Delta M^{(2)}$ for any choice can be calculated and compared with experiment. Inclusion of $J^{(2)}$ triplets, in addition to $J^{(2)}$ pairs, in the calculation of $\Delta M^{(2)}$ makes the comparison even more reliable.

Using the statistical tables in Ref. 3, the contribution of pairs and triplets to $\Delta M^{(2)}$ was calculated for each of the six possible choices of the DN associated with $J^{(2)}$. Only one of these choices agreed with the experimental value of $\Delta M^{(2)}$.

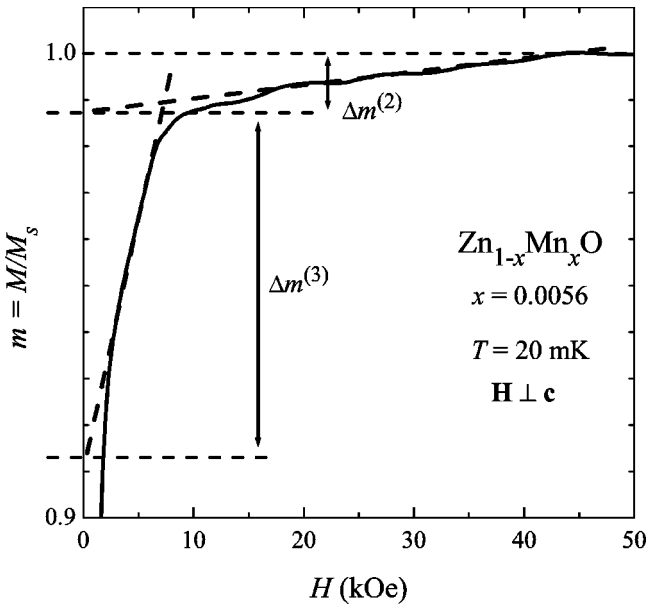

FIG. 7. Magnetization trace for $x=0.0056$, obtained at $T=20$ mK with $\mathbf{H}\perp\mathbf{c}$. The ordinate m is the magnetization M normalized to the technical saturation value M_s. This figure illustrates the procedure used to estimate the contribution $\Delta m^{(2)}$ to m from all $J^{(2)}$ clusters, and the contribution $\Delta m^{(3)}$ to m from all $J^{(3)}$ clusters.

Thus, a unique identification of the cluster class associated with $J^{(2)}$ was achieved. A similar procedure was also used for a preliminary identification of the DN responsible for $J^{(3)}$, but in that case two possible DN classes gave good agreement with experiment, so that a unique choice could not be made. The full numerical simulations, *for all the samples*, carried out at the end of the analysis, confirmed the preliminary identifications of the DN classes on the basis of the data for $x=0.0056$.

3. DN class responsible for $J^{(2)}$

The procedure of extracting the experimental ratio $\Delta m=\Delta M/M_s$ from the data, for the ramps associated with $J^{(2)}$ and $J^{(3)}$, is illustrated in Fig. 7. For the higher-field ramp, associated with $J^{(2)}$, it gives $\Delta M^{(2)}/M_s=1.3\%$ for $x=0.0056$. The theoretical value of $\Delta M^{(2)}/M_s$ is obtained by multiplying $(\Delta M^{(2)}/M_0)$ by (M_0/M_s). The first ratio depends on the DN class n that corresponds to $J^{(2)}$. For each possible n, this ratio was obtained from probability tables for pairs and triplets that involve only the exchange constant for class n.[3] The probabilities are based on a cluster model that includes only the two classes of NN's and the DN class n. The second ratio (M_0/M_s) was calculated from the so-called NN cluster model,[2] in which only the two classes of NN's are included.

For small x the calculated ratio of $\Delta M^{(2)}/M_s$ increases as the coordination number z_n increases. This dependence on z_n is the key for identifying the DN class that corresponds to $J^{(2)}$. For $x=0.0056$ the calculated values of $\Delta M^{(2)}/M_s$ are 1.39% for the only DN class with $z_n=2$, between 3.1% and 4.2% for the three possible classes with $z_n=6$, and 6.1% for the two possible classes with $z_n=12$. The experimental value

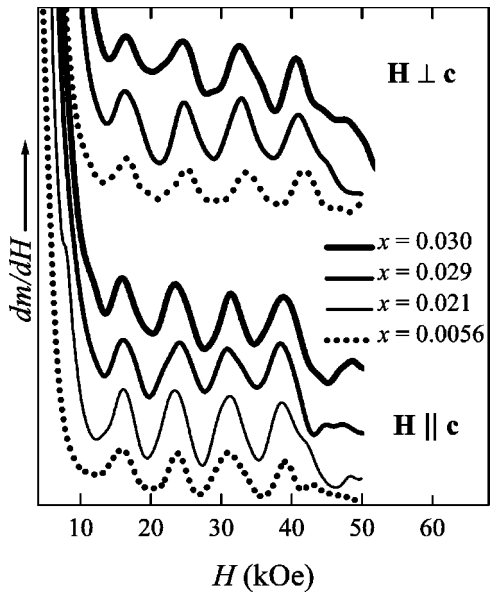

FIG. 8. Numerical derivatives dm/dH of $m \equiv M/M_s$, obtained from the experimental magnetization traces at 20 mK. The results are for two field directions: $\mathbf{H} \| \mathbf{c}$ and $\mathbf{H} \| [10\bar{1}0]$. The latter direction is designated as $\mathbf{H} \perp \mathbf{c}$. The sample with $x = 0.021$ has been measured only with $\mathbf{H} \| \mathbf{c}$. The traces have been displaced vertically relative to each other, but the gain is the same.

1.3% agrees only with $z_n = 2$, which corresponds to $n = 4$ in Table I. In the ideal wurtzite structure such a DN is reached from the ''central'' cation by moving a distance $r_4 = c = \sqrt{8/3}a$ along the c axis (see Fig. 1). In Table I the exchange constant $J(4)$ for $n = 4$ is designated as J_3'. It is noteworthy that this largest DN exchange constant is not for the DN that is closest to the central cation. The closest DN is of class $n = 3$, at a distance $r_3 = \sqrt{2}a$. Thus, the magnitudes of the exchange constants do not decrease monotonically with distance. This nonmonotonic dependence on distance was predicted by some theories,[11,12] and has been observed experimentally earlier.[5,20]

4. Values of J_3' and D

The values for J_3' and D were obtained from analysis of the well resolved MST's on the ramp associated with $J^{(2)} = J_3'$ [see Fig. 6(b)]. These MST's stand out more clearly in the derivative dm/dH of the normalized magnetization $m \equiv M/M_s$, shown in Fig. 8. For three of the four samples in this figure the data are for both $\mathbf{H} \perp \mathbf{c}$ and $\mathbf{H} \| \mathbf{c}$. The dependence of the fields at the MST's on field direction is caused by the anisotropy. Because the c axis is an easy axis ($D < 0$), the spins in the pairs are aligned more quickly for $\mathbf{H} \| \mathbf{c}$ than for $\mathbf{H} \perp \mathbf{c}$. The faster alignment for $\mathbf{H} \| \mathbf{c}$ is more apparent in part (b) of Fig. 6.

All curves in Fig. 8 show the last four MST's from J_3' pairs. For $x = 0.0021$ the first MST is also seen, but only as a ''shoulder'' on the fast drop of dm/dH at low fields. The fields at the last four MST's are all above 15 kOe. Values of both J_3' and D were obtained from an analysis of these fields, based on a pair Hamiltonian which included the exchange interaction due to J_3', the uniaxial anisotropy governed by D, and the dd interaction. The latter was calculated using the value in Table I for $n = 4$.

In the first step of the analysis, an approximate value for J_3' was obtained from the field at the last (fifth) MST, and the EPR value of D (Ref. 22) was adopted as the initial value. Later, the predicted fields at the last four MST's, for both field directions, were calculated for many sets of (J_3', D). The best match with the experimental values gave $J_3'/k_B = -0.543 \pm 0.005$ K and $D/k_B = -0.039 \pm 0.008$ K. The presumably more accurate EPR value for D/k_B is -0.031 K. The difference may be related to our use of the dd interaction constant given in Table I. As noted, this constant was obtained from a simple model in which the spins in a pair are represented by two points separated by r_4.

5. Possible DN classes associated with $J^{(3)}$

Possible assignments of the DN class which corresponds to $J^{(3)}$ were made on the basis of the magnitude $\Delta m^{(3)}$ in Fig. 7. The experimental results give $\Delta m^{(3)} = \Delta M^{(3)}/\Delta M_s \approx 7.3\%$ for $x = 0.0056$. This $\Delta m^{(3)}$ was attributed to the combined magnetization rise from pairs and triplets involving this exchange constant. The inclusion of triplets in the theoretical calculation of $\Delta m^{(3)}$ was more important than in the calculation of $\Delta m^{(2)}$, because the triplets/pairs population ratio was higher. The triplets/pairs ratio increases with z_n. The lowest possible coordination number, $z_n = 2$, is for the neighbor class $n = 4$ associated with $J^{(2)}$ and $\Delta m^{(2)}$.

Theoretical values of $\Delta m^{(3)}$ were obtained from cluster models which included the three largest exchange constants (J_1, J_1', J_3') and any one of the DN classes with either $z_n = 6$ or $z_n = 12$. The calculated values are approximately 3.1% for all three DN classes with $z_n = 6$ and approximately 6.0% for the two DN classes with $z_n = 12$. On this basis, z_n is equal to 12, which leads to two possible neighbor classes: $n = 6$ or $n = 7$ (see Table I). That is, $J^{(2)}$ is either J_3^{out} or J_4'. Another possibility (unlikely, but cannot be ruled out entirely) is that $J^{(3)}$ is associated with two different classes, both with $z_n = 6$, that just happen to have very nearly equal exchange constants.

6. Value of $J^{(3)}$

Figure 9 displays dm/dH data for both $\mathbf{H} \| \mathbf{c}$ and $\mathbf{H} \perp \mathbf{c}$, in the field range relevant for the analysis of $J^{(3)}$. Due to the smallness of $J^{(3)}$, the effects of the anisotropy are important, as can be judged from the strong dependence of the results on the direction of $\mathbf{H}$. The dm/dH traces for $\mathbf{H} \| \mathbf{c}$, in Fig. 9(a), do not show the regular sequence of peaks observed in Fig. 8 for the MST's from J_3' pairs. However, all traces in Fig. 9(a) show a peak slightly above 2 kOe. The best resolution is for the sample with $x = 0.021$. In this sample, two additional peaks, just below and just above 4 kOe, are also resolved.

The results in Fig. 9 were compared with simulations based on a pair Hamiltonian which included $J^{(3)}$ and the two anisotropies. The simulations used $D/k_B = -39$ mK, as determined in Sec. VI C 4, and the dd interaction constant

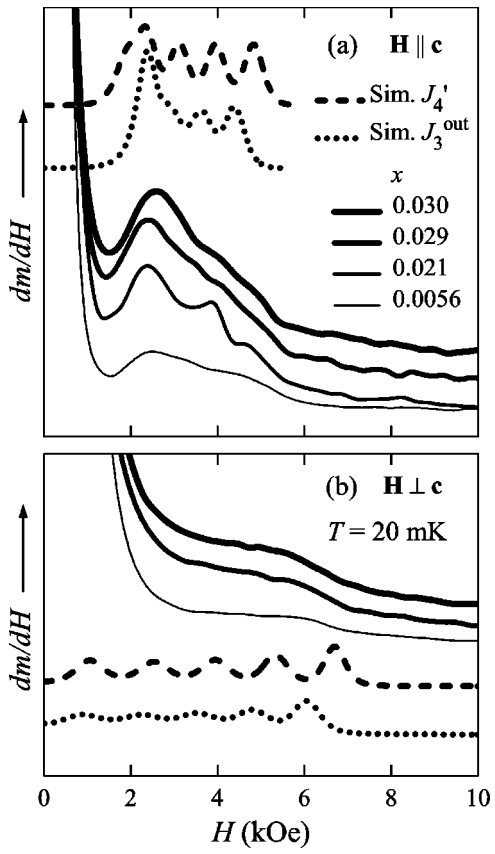

FIG. 9. Low-field portion of the dm/dH data with (a) $\mathbf{H}\|\mathbf{c}$ and (b) $\mathbf{H}\perp\mathbf{c}$. Different experimental traces are displaced vertically from each other, but the gain is the same. Also shown are simulations for the two types of pairs involving the two classes of neighbors with $z_n=12$. The heavy dashed lines are for pairs with exchange constant J_4' between the central cation and a neighbor of the class $n=7$. The dotted lines are for pairs with J_3^{out}, involving a neighbor of the class $n=6$. The simulations are for the actual temperature $T=20$ mK, and they include the single-ion anisotropy, involving D, and the dd anisotropy.

taken from Table I. Because the latter constant depends on the DN class, simulations were carried out for the two possible neighbor classes with $z_n=12$, i.e., $n=6$ with J_3^{out}, and $n=7$ with J_4'.

For $\mathbf{H}\perp\mathbf{c}$, pairs involving neighbors of either class have different orientations relative to $\mathbf{H}$. The different orientations lead to different energies from the dd anisotropy, and they give rise to MST's at slightly different fields. Therefore, in the simulations for the perpendicular field direction, $\mathbf{H}\|[10\bar{1}0]$, pairs involving DN's of either of the two possible classes were divided into groups. Pairs in different groups had different orientations relative to $\mathbf{H}$. There were three such groups for the DN class $n=6$, with J_3^{out}, and two groups for $n=7$, with J_4'. The simulated magnetization curve was obtained by adding the results from all the groups.

The simulations were carried out using the actual temperature, $T=20$ mK. Nonthermal broadening mechanism, such as local strains that give rise to a spread of the exchange and anisotropy interactions,[39] were ignored. In these simulations the values $D/k_B=-39$ mK, and the dd interaction constant from Table I, were kept fixed. The value of $J^{(3)}$ was adjusted to obtain the best match with experiment for both field orientations. The final dm/dH simulations are shown in Figs. 9(a) and 9(b) as the dashed and dotted lines. Obviously, the results of the simulations depend on field direction. For $\mathbf{H}\|\mathbf{c}$, the overall structure of the experimental dm/dH traces is reproduced by the simulations. However, because some sources of line broadening were neglected in the simulations, the detailed structure is better resolved in the simulations than in the experimental curves. For $\mathbf{H}\perp\mathbf{c}$ the individual MST's are resolved in the simulations, even after the different orientations of the pairs relative to H are included. Experimentally, however, the individual MST's are not resolved for $\mathbf{H}\perp\mathbf{c}$. This difference is attributed, again, to the neglect of some broadening mechanisms in the simulations. A crude way of accounting for the neglected broadening mechanisms is to replace the actual temperature T in the simulations by a higher effective temperature T_{eff}. The minimum T_{eff} which leads to unresolved MST's for $\mathbf{H}\perp\mathbf{c}$ is 65 mK.

Some features of the experimental data in Figs. 9(a) and 9(b) are sensitive to the magnitude of $J^{(3)}$. For $\mathbf{H}\|\mathbf{c}$ these features include the field at the most prominent peak, and the field at the peak associated with the last MST. These peaks stand out most clearly in the trace for $x=0.021$. For $\mathbf{H}\perp\mathbf{c}$ the field at the rapid drop of dm/dH, which is at the end of the ramp associated with this series of MST's, is sensitive to the value of $J^{(3)}$. The value of $J^{(3)}$ was determined from comparisons of these experimentally observed features with simulations that used different values of $J^{(3)}$. Assuming that $J^{(3)}$ is J_3^{out}, the results gave $J^{(3)}/k_B=-0.074\pm0.005$ K. The alternative $J^{(3)}=J_4'$ gave -0.082 ± 0.005 K. The first choice gives a slightly better agreement with the data, but in our view the evidence is insufficient for concluding that the DN class is definitely J_3^{out}.

7. Simulations with both DN exchange constants

Simulations of the magnetization curves, in fields up to 60 kOe, were carried out in order to confirm the preliminary identifications of the DN classes corresponding to $J^{(2)}$ and $J^{(3)}$. The simulations were for all samples, in contrast with the preliminary analysis that was carried out only for the sample with the lowest Mn concentration, $x=0.0056$. The simulations used cluster models which included the two NN exchange constants (J_1 and J_1'), $J^{(2)}$ and $J^{(3)}$, all having the values quoted above. Each cluster model was based on a specific choice of the two DN classes associated with $J^{(2)}$ and $J^{(3)}$. As noted earlier, there are 30 possible such choices. The results of the simulations were not sensitive to any change of the DN class n, provided that the coordination number z_n did not change.

Because all anisotropies were neglected in the simulations, the comparison was made with ''isotropic'' magnetization curves obtained from the experimental data using the relation

$$M_{\text{isot}}=(M_{\|}+2M_{\perp})/3, \tag{2}$$

where $M_{\|}$ is for $\mathbf{H}\|\mathbf{c}$, and $M_{\perp}$ is for $\mathbf{H}\perp\mathbf{c}$. The widths of the MST's exhibited by M_{isot} are larger than the thermal width at

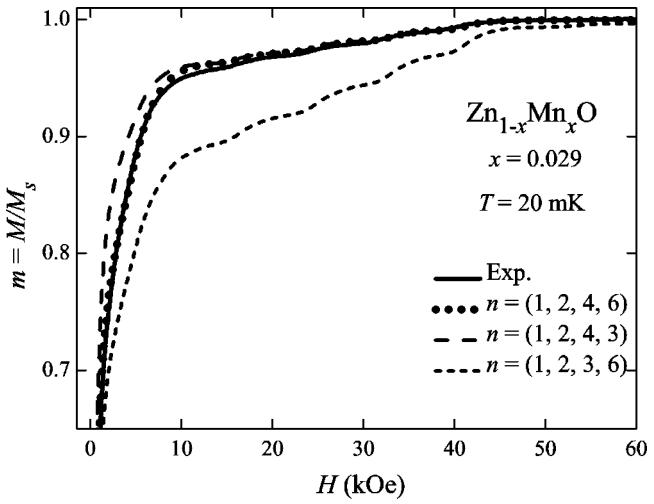

FIG. 10. Comparison between the isotropic ''experimental'' magnetization $M_{\rm isot}=(M_{\parallel}+2M_{\perp})/3$, (see text) and numerical simulations based on the four exchange constants associated with the neighbor classes $n=i,j,k,l$. The simulations assume a random distribution of the Mn ions, and an effective temperature $T_{\rm eff}=100$ mK.

20 mK for several reasons. First, $M_{\rm isot}$ is an average over different groups of pairs with MST's at slightly different fields. Second, DN exchange constants smaller than $J^{(3)}$ were neglected. Third, variations of the J's, and of the anisotropies, caused by local strains[39] were not included. To match the widths of the MST's on the ramp which ends at 40 kOe, the simulations were carried out using an effective temperature $T_{\rm eff}=100$ mK instead of 20 mK. This change has no effect on the identification of the DN's responsible for $J^{(2)}$ and $J^{(3)}$; the only effect is to smooth the curves. Simulations using the actual temperature, 20 mK, lead to the same identifications of the DN classes.

Figure 10 shows simulations for $x=0.029$. The ''experimental'' curve represents $M_{\rm isot}$. Each simulation is labeled as $n=(i,j,k,l)$. This designation means that the four exchange constants $J_1, J_1', J^{(2)}$, $J^{(3)}$ that were used in the simulation, correspond, respectively, to the neighbor classes $n=i,j,k,l$ in Table I. All the simulations assumed that the first two neighbor classes (i,j) were those of the NN's, that is, $(i,j)=(1,2)$ or $(2,1)$. (These two alternative choices are related to each other by an interchange of the NN classes assigned to J_1 and J_1'.) Both choices lead to nearly the same curves in this field range. The best agreement is with the simulation $n=(1,2,4,6)$ in which $J^{(2)}=J_3'$ and $J^{(3)}=J_3^{\rm out}$. This corresponds to one of the two possibilities which were identified earlier. The other possibility $n=(1,2,4,7)$, not shown in Fig. 10, leads to a very similar curve, so that a definite unique choice of the DN class for $J^{(3)}$ is not possible.

The same conclusions concerning the neighbor classes associated with $J^{(2)}$ and $J^{(3)}$ were reached from comparisons of the data for the other samples ($x=0.0056$, $x=0.021$, and $x=0.030$) with simulations. Thus, the earlier identifications of the DN classes are confirmed. The good agreement between the data and the simulations also lends support to a random Mn distribution in the studied samples, which is the main assumption in the simulations.

ACKNOWLEDGMENTS

The work in Brazil was supported by FAPESP (Fundação de Amparo à Pesquisa do Estado de São Paulo, Brazil) under Contract No. 99/10359–7. The work in Poland was supported by Grant No. PBZ-KBN-044/P03/2001. V.B. and N.F.O.J. acknowledge support from CNPq (Conselho Nacional de Desenvolvimento Científico e Tecnológico, Brazil). Travel funds for Y.S. were provided by FAPESP.

*Electronic address: vbindilatti@if.usp.br
†Electronic address: yshapira@granite.tufts.edu

[1] See, e.g., in *Semimagnetic Semiconductors and Diluted Magnetic Semiconductors*, edited by M. Averous and M. Balkanski (Plenum, New York, 1991); in *Diluted Magnetic Semiconductors*, edited by J.K. Furdyna and J. Kossut, Semiconductors and Semimetals Vol. 25 (Academic, New York, 1988); T. Dietl, in *Handbook on Semiconductors*, edited by T.S. Moss (North-Holland, Amsterdam, 1994), Vol. 3b, p. 1251.

[2] Y. Shapira and V. Bindilatti, J. Appl. Phys. **92**, 4155 (2002).

[3] See EPAPS Document No. E-JAPIAU-92-110220 For the cluster tables which accompany Ref. 2. A direct link to this document may be found in the online article's HTML reference section. The document may also be reached via the EPAPS homepage (http://www.aip.org/pubservs/epaps.html) or from ftp.aip.org in the directory /epaps/. See the EPAPS homepage for more information.

[4] S. Foner, Y. Shapira, D. Heiman, P. Becla, R. Kershaw, K. Dwight, and A. Wold, Phys. Rev. B **39**, 11 793 (1989).

[5] V. Bindilatti, E. ter Haar, N.F. Oliveira, Jr., Y. Shapira, and M.T. Liu, Phys. Rev. Lett. **80**, 5425 (1998).

[6] H. Malarenko, Jr., V. Bindilatti, N.F. Oliveira, Jr., M.T. Liu, Y. Shapira, and L. Puech, Physica B **284-288**, 1523 (2000).

[7] Y. Shapira, S. Foner, D. Heiman, P.A. Wolff, and C.R. McIntyre, Solid State Commun. **71**, 355 (1989).

[8] V. Bindilatti, T.Q. Vu, Y. Shapira, C.C. Agosta, E.J. McNiff, Jr., R. Kershaw, K. Dwight, and A. Wold, Phys. Rev. B **45**, 5328 (1992).

[9] R.A. Cajacuri, X. Gratens, E. ter Haar, V. Bindilatti, N. Oliveira, Jr., Y. Shapira, and Z. Golacki, J. Magn. Magn. Mater. **226-230**, 1981 (2001).

[10] B.E. Larson, K.C. Haas, H. Ehrenreich, and A.E. Carlsson, Phys. Rev. B **37**, 4137 (1988); **38**, 7842(E) (1988).

[11] S.S. Yu and V.C. Lee, Phys. Rev. B **52**, 4647 (1995).

[12] S. Wei and A. Zunger, Phys. Rev. B **48**, 6111 (1993).

[13] For an early review see T.M. Giebultowicz, J.J. Rhyne, J.K. Furdyna, and P. Klosowski, J. Appl. Phys. **67**, 5096 (1990),

[14] L.M. Corliss, J.M. Hastings, S.M. Shapiro, Y. Shapira, and P. Becla, Phys. Rev. B **33**, 608 (1986); T.M. Giebultowicz, J.J. Rhyne, and J.K. Furdyna, J. Appl. Phys. **61**, 3537 (1987).

[15] H. Kępa, V.K. Le, C.M. Brown, M. Sawicki, J.K. Furdyna, T.M.

Giebultowicz, and T. Dietl, Phys. Rev. Lett. **91**, 087205 (2003).
[16] T. Dietl, H. Ohno, F. Matsukura, J. Cibert, and D. Ferrand, Science **287**, 1019 (2000).
[17] S.W. Jung, S.J. An, G.C. Yi, C.U. Jung, S.I. Lee, and S. Cho, Appl. Phys. Lett. **80**, 4561 (2002).
[18] T. Fukumura, Z. Jin, M. Kawasaki, T. Shono, T. Hasegawa, S. Koshihara, and H. Koinuma, Appl. Phys. Lett. **78**, 958 (2001).
[19] V. Ladizhansky, A. Faraggi, V. Lyahovitskaya, and S. Vega, Phys. Rev. B **56**, 6712 (1997).
[20] B. Hennion, W. Szuszkiewicz, E. Dynowska, E. Janik, and T. Wojtowicz, Phys. Rev. B **66**, 224426 (2002).
[21] B.E. Larson, K.C. Hass, and R.L. Aggarwal, Phys. Rev. B **33**, 1789 (1986).
[22] P.B. Dorain, Phys. Rev. **112**, 1058 (1958).
[23] Y. Shapira, J. Appl. Phys. **67**, 5090 (1990).
[24] V. Bindilatti, N.F. Oliveira, Jr., E. ter Haar, and Y. Shapira, Czech. J. Phys. **46**, 3255 (1996).
[25] X. Gratens, V. Bindilatti, E. ter Haar, N.F. Oliveira, Jr., Y. Shapira, and F.C. Montenegro, Phys. Rev. B **64**, 214424 (2001).
[26] S. Foner, Physica B **201**, 13 (1994).
[27] Y. Shapira, M.T. Liu, S. Foner, C.E. Dube, and P.J. Bonitatebus, Phys. Rev. B **59**, 1046 (1999).
[28] Y. Shapira, M.T. Liu, S. Foner, R.J. Howard, and W.H. Armstrong, Phys. Rev. B **63**, 094422 (2001).
[29] Y. Ajiro, T. Asano, H. Aruga-Katori, T. Goto, K. Koui, K. Kamishima, and H. Ikeda, Physica B **246-247**, 222 (1998).
[30] Additional evidence that these MST's are from the two dominant exchange constants associated with the NN's comes from values of the Curie-Weiss temperature θ. These values, obtained both in the present study and in Ref. 18, lead to a dominant AF exchange constant which agrees with the more accurate values obtained here within 30%.
[31] B.E. Larson, J. Appl. Phys. **67**, 5240 (1990).
[32] B.E. Larson and H. Ehrenreich, Phys. Rev. B **39**, 1747 (1989).
[33] W. Wernsdorfer, S. Bhaduri, R. Tiron, D.N. Hendrickson, and G. Christou, Phys. Rev. Lett. **89**, 197201 (2002).
[34] A. Paduan-Filho, N. F. Oliveira, Jr., V. Bindilatti, S. Foner, and Y. Shapira, Phys. Rev. B **68**, 224417 (2003).
[35] H. Nakano and S. Miyashita, J. Phys. Soc. Jpn. **70**, 2151 (2001); K. Saito and S. Miyashita, *ibid.* **70**, 3385 (2001); H. Nakano and S. Miyashita, J. Phys. Chem. Solids **63**, 1519 (2002).
[36] O. Waldmann, R. Koch, S. Schromm, P. Müller, I. Bernt, and R.W. Saalfrank, Phys. Rev. Lett. **89**, 246401 (2002); **90**, 229904(E) (2003).
[37] I. Chiorescu, W. Wernsdorfer, A. Müller, H. Bögge, and B. Barbara, Phys. Rev. Lett. **84**, 3454 (2000); I. Chiorescu, W. Wernsdorfer, A. Müller, S. Miyashita, and B. Barbara, Phys. Rev. B **67**, 020402 (2003).
[38] Y. Inagaki, T. Asano, Y. Ajiro, Y. Narumi, K. Kindo, A. Cornia, and D. Gatteschi, J. Phys. Soc. Jpn. **72**, 1178 (2003).
[39] Y.G. Rubo, M.F. Thorpe, and N. Mousseau, Phys. Rev. B **56**, 13 094 (1997).